

Self-ordering induces multiple topological transitions for in-plane bulk waves in solid phononic crystals

Jiujiu Chen,^{1,*} Hongbo Huang,¹ Shaoyong Huo,¹ Zhuhua Tan,^{2,†} Xiaoping Xie,¹ Jianchun Cheng,^{3,‡} and Guo-liang Huang⁴

¹*State Key Laboratory of Advanced Design and Manufacturing for Vehicle Body, College of Mechanical and Vehicle Engineering, Hunan University, Changsha 410082, China*

²*School of Mechanical Engineering, Hebei University of Technology, Tianjin 300401, China*

³*Department of Physics, Nanjing University, Nanjing 210093, China*

⁴*Department of Mechanical and Aerospace Engineering, University of Missouri, Columbia, Missouri 65211, USA*



(Received 22 April 2018; published 10 July 2018)

Topological defects with symmetry-breaking phase transitions have captured much attention. A vortex generated by topological defects exhibits exotic properties, and its flow direction can be switched by altering the spin configurations. Contrary to electromagnetic and acoustic domains, the topological transport of in-plane bulk waves in periodic structures with topological defects is not well explored due to the mode conversion between longitudinal and transverse modes. Here, we propose an elastic topological insulator with spontaneously broken symmetry based on the topological theory of defects and homotopy theory. Multiple topological transitions for in-plane bulk waves are achieved by topologically modifying the ellipse orientation in a triangular lattice of elliptical cylinders. The solid system, independent of the number of molecules in order-parameter space, breaks through the limit of point-group symmetry to emulate elastic pseudospin-orbit coupling. The transport robustness of the edge states is experimentally demonstrated. Our approach provides new possibilities for controlling and transporting in-plane bulk waves.

DOI: [10.1103/PhysRevB.98.014302](https://doi.org/10.1103/PhysRevB.98.014302)

I. INTRODUCTION

Topological defects in ordered media [1] with spontaneously broken symmetry have attracted an enormous interest due to their nontrivial topology, which can play a central role in physical processes such as phase transitions [2–4]. Their topological origin and fundamental behavior was first described by the Kibble-Zurek mechanism as a continuous system is quenched across a phase transition into an ordered state [5,6]. In recent years, such topological defects have been extensively studied in various branches of physics. It has been shown that the topological defects with $+1/2$ or $-1/2$ topological charge can govern cell motion [7–9], and even arise in fatigue of materials [10]. Antivortices and vortices can be generated in three-dimensional nonporous ferroelectric structures with topological defects [11]. These exotic physical phenomena and unprecedented material properties imply that topological defects can be leveraged to explore quantum behavior of classical waves and new forms of topological orders in condensed-matter systems.

The discovery of topologically ordered states is an exciting field of research inspired by quantum systems. Since then, the concept has been extended to other areas, including photonics [12–25] and acoustics [26–40]. It has also given an impetus to find a new way to design elastic systems [41–59]. Compared with other classical waves, elastic wave motion in solid media

has three polarizations (one longitudinal and two transverse modes) [41]. The unique properties enrich the investigations into new topologically protected edge states based on multiple effective modes, such as bulk waves [43,56–59], Lamb waves [41,54,55], and flexural waves [48–53]. Given that the nature of Fermi electrons is fundamentally different from bosonic phonons, there are two ways to realize topologically protected wave propagation in elastic media. One possible way is to emulate the quantum Hall effect [42–45] by breaking the time-reversal symmetry. Another alternative is to employ solely passive components to establish analogs of the quantum valley Hall effect [48–52,57] and the quantum spin Hall effect [53–56,58,59]. While recent numerical studies have successfully realized the quantum spin Hall phase transition for in-plane bulk waves [58,59], the experimental observation of such topological wave propagation in solid phononic crystals (PCs) has not yet been explored due to the existence of both transverse and longitudinal polarizations. Moreover, these systems have high modal densities and large acoustic impedance mismatch, making them vulnerable to structure defects and enhancing strong backscattering at the boundaries between distinct materials. Thus, these challenges have hindered the experimental realization of topological protection for in-plane bulk waves on an integrated platform.

In this article, we introduce the concept of topological defects to a triangular lattice of elliptical cylinders, and we demonstrate experimentally the topologically protected helical edge states for in-plane bulk waves in solid PCs with spontaneously broken symmetry. The ellipse orientations vary spatially to create topological defects in the orientational order, which induces the vortex chirality (i.e., right- or

*jjchen@hnu.edu.cn

†zhtan@hnu.edu.cn

‡jccheng@nju.edu.cn

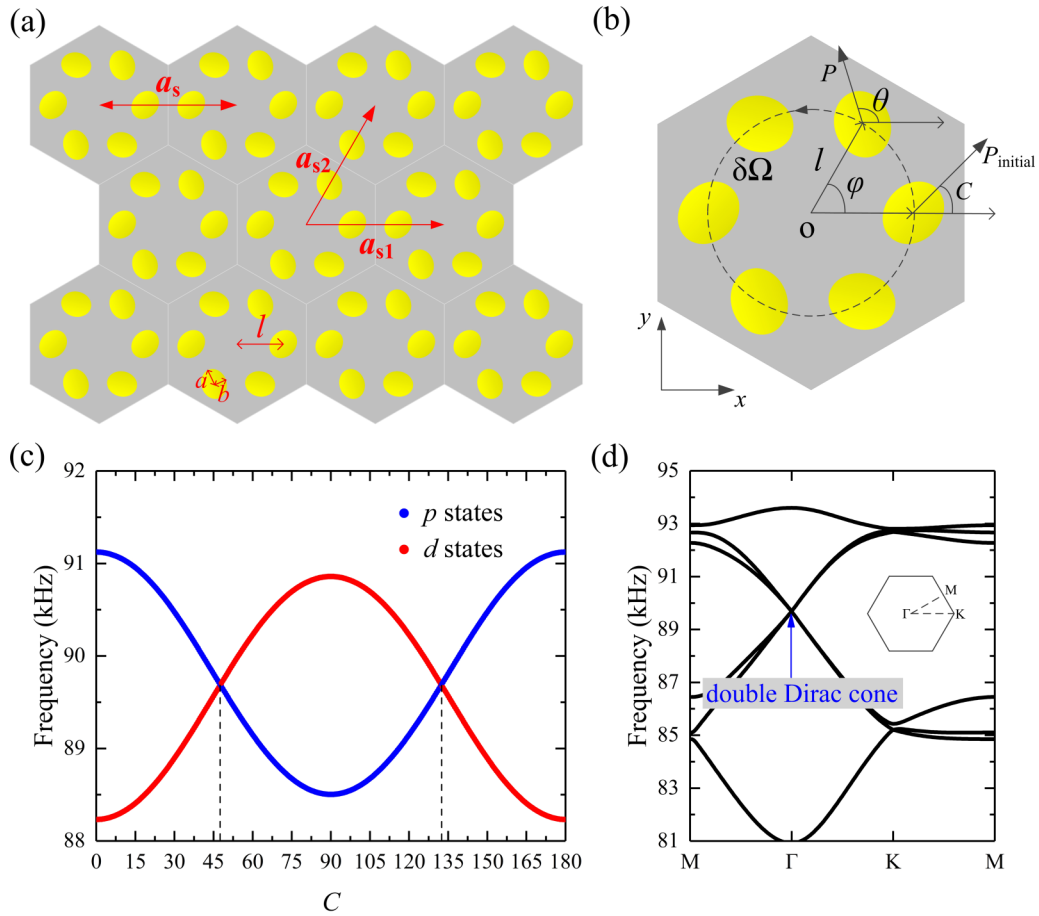


FIG. 1. (a) Schematic illustration of a triangular lattice of hexagonal clusters composed of six elliptical cylinders embedded in an epoxy resin. (b) Unit-cell diagram and order-parameter space of the PCs. (c) Eigenfrequencies of the p - and d -type states at the Γ point evolving for a sweep of the initial phase C . (d) Calculated band structure in which $C = 47.5^\circ$ and 132.5° , showing the fourfold-degenerate double Dirac cone at the Γ point. (Inset: Brillouin zone of triangular lattice.)

left-hand circular polarized, labeled as RCP and LCP), thereby resulting in multiple topological transitions between trivial and topological phononic bands. Our proposal opens a whole new realm of research and technological opportunities to acquire elastic topological phases without relying on tuning the filling ratio or folding the Brillouin zone, and it paves the way for the design of a unique topological insulator without the limit of point-group symmetry and the lattice structure, which may serve as a prototype for future development of elastic wave devices.

II. DESIGN

To start with, we consider a triangular lattice of elliptical tungsten cylinders embedded in an epoxy resin [Fig. 1(a)]. The lattice constant is $a_s = 15$ mm and the distance between the center of each cluster to the centroid of each ellipse is $l = a_s/3$. The major axis of the ellipse is $a = 1.644$ mm and the minor axis is $b = 1.370$ mm. In the following, the theory of topological defects [1–3] is used to describe the elementary topology of the PCs by rotating individual ellipses in a unit cell in different directions. As schematically shown in Fig. 1(b), the orientational modification can be mapped on the order parameter space θ , which is defined as the angle between the

major axis of an ellipse and the given x axis, and it is written as [1]

$$\theta = k\varphi + C, \quad (1)$$

where $\varphi = \tan^{-1}(y/x)$ represents the polar angle of the center position of the ellipse, and C is the initial phase for $\varphi = 0$. The integer k is the topological charge and is equivalent to the winding number n . It is calculated by measuring the total rotation in θ -space and can be defined by $n = \oint_{\delta\Omega} \nabla\theta \cdot dL$, where $\delta\Omega$ denotes a closed contour and $L(l, \varphi)$ denotes the polar coordinates. Note that the topological modification structure is characterized by the winding number and the initial phase, in which the winding number is used to classify different homotopy classes while the initial phase is used to distinguish between the modification structures in each homotopy class. Due to the symmetry of θ -space in our system, n can take on the values of $+1, 0$. Herein, $n = +1$ with respect to the vortex and hedgehog structure, and $n = 0$ with respect to trivial rectilinear modification structures. The ellipse-shaped cylinders are anisotropic, and the use of the initial phase enables the system to exhibit different symmetries. Thus, these structures, as a topological modification in the orientational

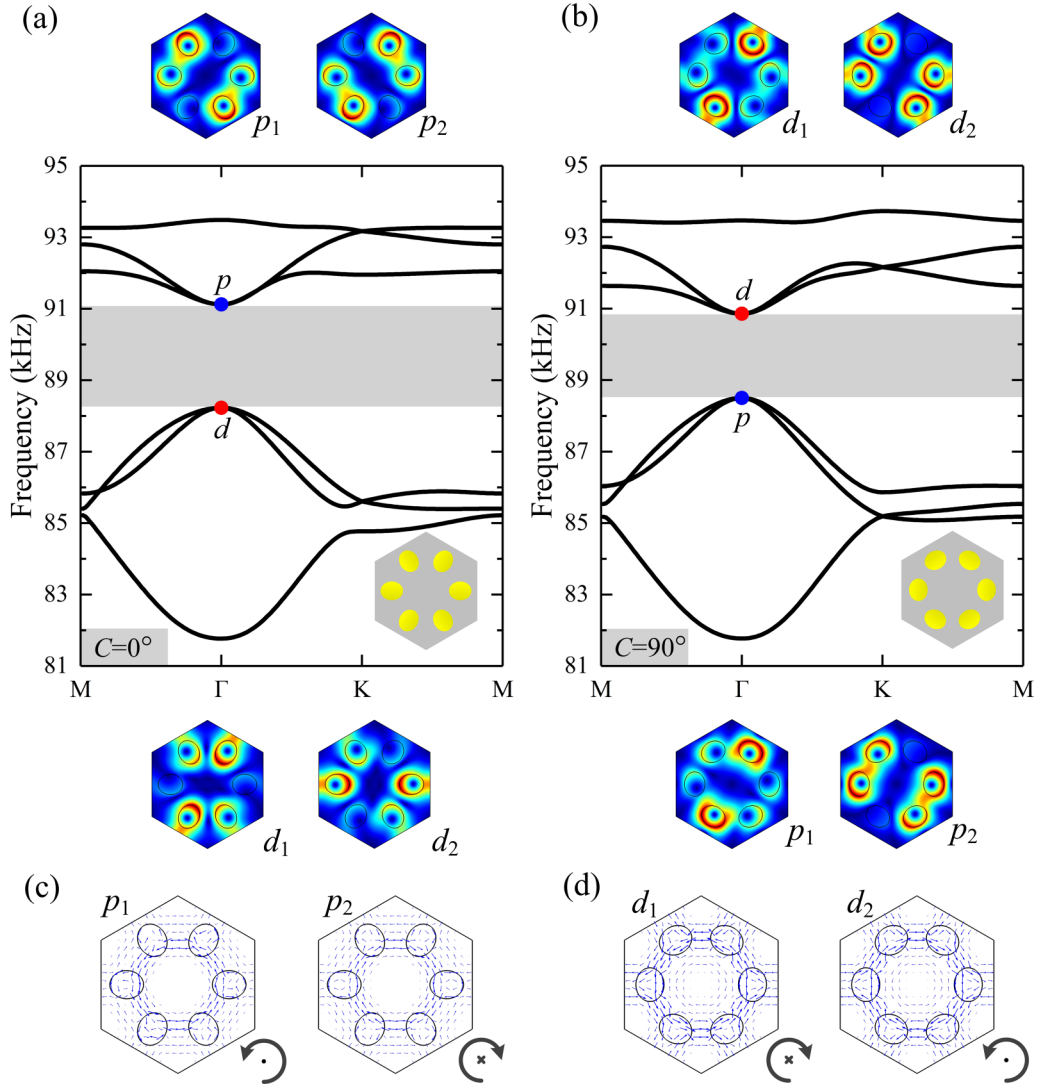


FIG. 2. Band structures of the solid PCs with different initial phase. Unit cells are depicted at the bottom right corner in each subfigure. Panel (a) represents the radical configuration with the initial phase $C = 0^\circ$ and the associated displacement field distributions for the degenerated eigenstates at the Γ point. Panel (b) represents the azimuthal configuration with the initial phase $C = 90^\circ$; the p - and d -type states are inverted with respect to the band gap, which indicates the occurrence of band inversion. The band gap (gray shaded region) in (a) is topologically nontrivial, whereas the one in (b) corresponds to a topologically trivial regime. The time-averaged mechanical energy flux (indicated by the blue arrows) associated with the pseudospin-up and pseudospin-down state around the Γ point above the band gap in the nontrivial regime (c) and the trivial regime (d).

order, markedly change the topological properties of the solid PCs and can be used to emulate the elastic pseudospin-orbit coupling.

III. MULTIPLE TOPOLOGICAL TRANSITIONS

According to the topological theory of defects and homotopy theory [1–3], the $n = +1$ structure is characterized by the nature of topological stability. To reveal the characteristics of the topological modification structure with $n = +1$ and create an elastic topological insulator for in-plane bulk waves, we demonstrate that the spatially inhomogeneous variation of the ellipse orientation can pose enhanced control over the topological phase, causing energy band inversion. Figure 1(c) shows the eigenfrequency spectra of p -type and d -type states at the Brillouin zone center evolving for a sweep of the initial

phase C . It is observed that the doubly degenerate band-edge frequencies vary smoothly and the eigenstates exchange occurs at $C = 47.5^\circ$ and 132.5° , resulting in a double Dirac cone with a fourfold accidental degeneracy at the Brillouin zone center. As can be seen, the solid PCs studied here have a broken continuous symmetry and undergo a symmetry inversion in reciprocal space, which ultimately induces multiple topological phase transitions. With inherent time-reversal invariants, the rotation of the crystalline domains introduces chirality to the structures with $C = 47.5^\circ$ and 132.5° , implying that the corresponding band structures are exactly the same, as illustrated in Fig. 1(d). The phononic band structures of in-plane bulk waves are calculated by solving the dispersion equation $[\mathbf{K}(\mathbf{k}) - \omega^2 \mathbf{M}]\mathbf{U} = \mathbf{0}$ for wave vector \mathbf{k} within the first irreducible Brillouin zone, where \mathbf{K} and \mathbf{M} denote the stiffness matrix and mass matrix, respectively [58]. It is worth

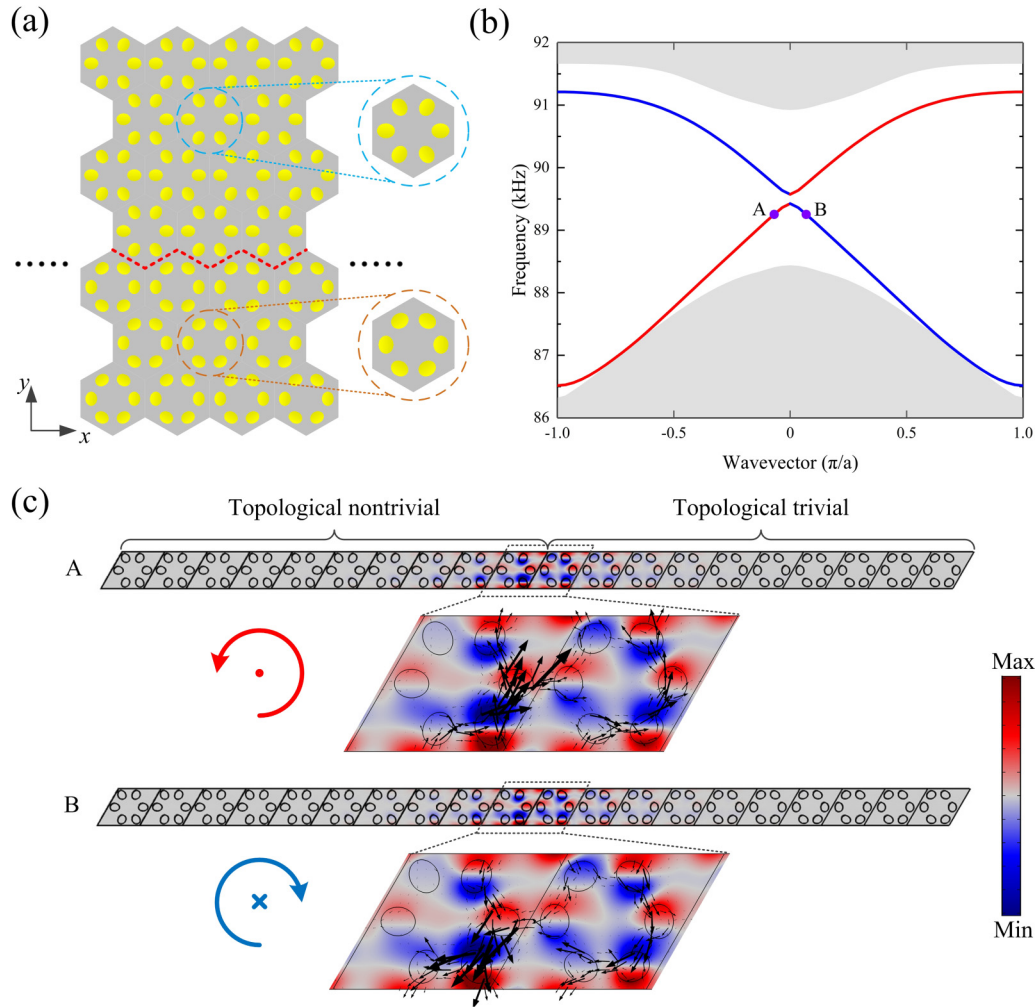


FIG. 3. (a) Schematic of the elastic topologically protected domain wall, in which the radical configuration is replicated at the upper domain wall, and the azimuthal configuration is replicated at the lower domain wall, respectively. The domain wall is marked by the dashed red line. (b) Calculated band structure for a 1×20 supercell with a domain wall at the center. The blue and red lines represent edge states of opposite group velocities, while the shaded regions indicate the bulk states. (c) The corresponding displacement field distribution of A and B states. Black arrows indicate the time-averaged mechanical energy flux.

noting that the four degeneracy bands constructed double Dirac cones are the mixed longitudinal-transverse polarization modes dominated by transverse polarization (see Appendix A for details).

We then introduce a perturbation to emulate elastic pseudospin-orbit coupling, accompanied by the opening of a topological band gap at the Γ point. To this end, the fourfold degeneracy needs to be lifted and split into two twofold-degenerate states. Figures 2(a) and 2(b) show the band structures of the radical configuration with $C = 0^\circ$ and the azimuthal configuration with $C = 90^\circ$, respectively. Seen in the insets are the associated displacement field distributions of the degenerate elastic eigenstates at the Brillouin zone center, which correspond, respectively, to the colored dots at the Γ point. The elastic spin-1/2 states can thus be realized through hybridizing the p/d states as $p_{\pm} = (p_1 \pm i p_2)/\sqrt{2}$ and $d_{\pm} = (d_1 \pm i d_2)/\sqrt{2}$, which is protected by a pseudo-time-reversal operator T ($T^2 = -1$). To elucidate the intrinsic physics of the elastic pseudospin states, we plot the time-averaged mechanical energy flux ($I_j = -\sigma_{ij} v_j$, where σ_{ij} and

v_j are the stress tensor and the velocity vector, respectively) around the Γ point above the band gap in the radical and azimuthal configuration, as illustrated in Figs. 2(c) and 2(d), respectively. It is observed that the rotation of the crystalline domains introduces the RCP/LCP chirality, which plays the role of the pseudospin degree of freedom. The vortex chirality corresponding to the pseudospin-up and pseudospin-down state is inverted by varying the initial phase C , which signals a topological phase transition. It is emphasized that the energy vortex is induced by the topological defects, and its flow direction can be switched by changing the ellipse orientation, which is essentially different from the realization of acoustic pseudospin states considered before [33]. Then, we present how band inversion takes place under the spatial variation of the ellipse orientation. For the radical configuration shown in Fig. 2(a), the two bands below the gap are of d -type, whereas the two bands above are p -type as per the analogy to electronic orbital shapes. For the azimuthal configuration shown in Fig. 2(b), the band gap still exists, however the positions of p and d are now inverted, i.e., p -type states are

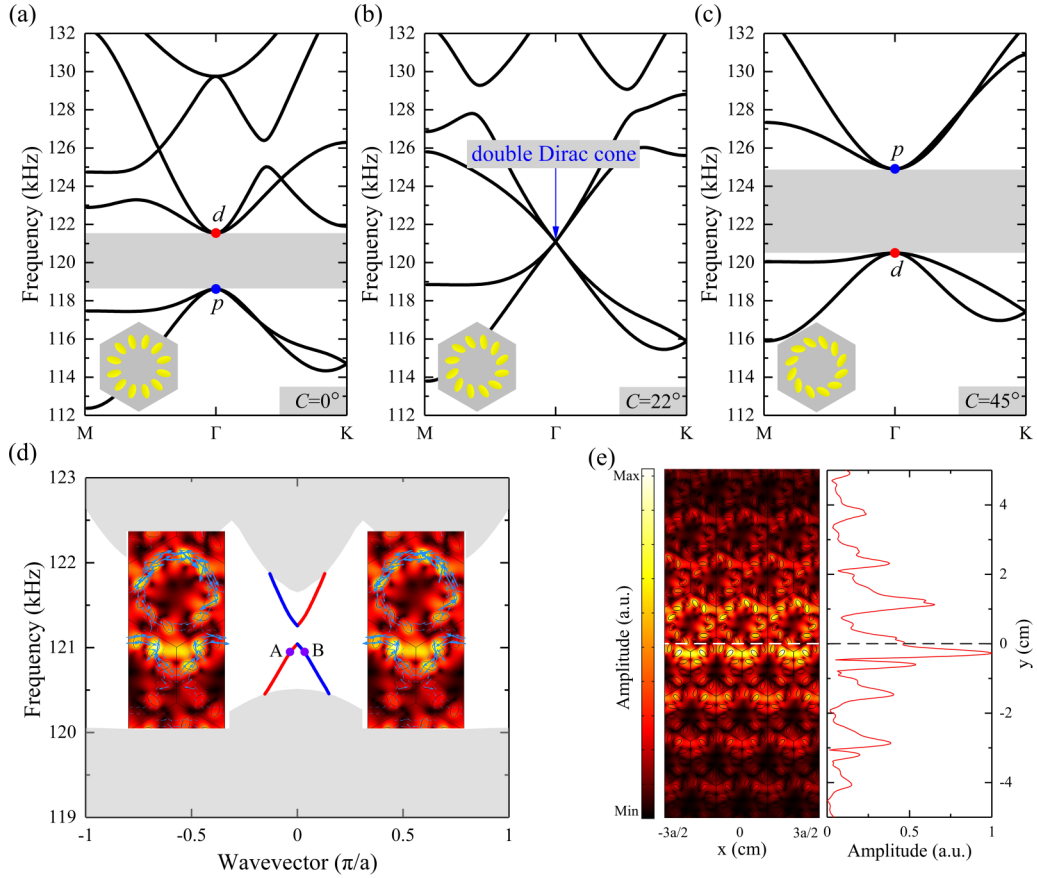


FIG. 4. (a)–(c) Band structures of the solid PCs with different initial phases with $C = 0^\circ$, 22° , and 45° , respectively. Unit cells are depicted at the bottom left corner in each subfigure. (d) Calculated band structure of a supercell consisting of a topological nontrivial crystal ($C = 45^\circ$) stacked with a topological trivial crystal ($C = 0^\circ$). The blue and red lines represent an elastic spin+ and spin− edge state, respectively. The inset shows the corresponding energy flux profiles for the edge modes, indicated by the blue arrows. The shaded regions indicate the bulk states. (e) Spatial amplitude profile of the displacement fields localized at the domain wall.

at the lower frequency compared to d -type states. Such a band inversion leads to a topological phase transition that occurs as the gap reopens, which is characterized by a nonzero Z_2 topological invariant. To determine the topology of the band gaps, we employ the $\mathbf{k} \cdot \mathbf{P}$ perturbation method [32,33,35,58] to calculate the spin Chern numbers. As expected, we obtain the spin Chern numbers $C_s = \pm 1$ in the case of the radical configuration, indicating that the band gap in Fig. 2(a) is nontrivial in topology. In contrast, the azimuthal configuration has the spin Chern numbers $C_s = 0$, which signify a topologically trivial band gap in Fig. 2(b). These results further confirm the appearance of a phase transition from nonzero Chern numbers to zero Chern numbers in two structures. Considering the broad generality in practical systems, we demonstrate that the topological modification in the orientational order is also applicable to other classic waves, such as solid-in-air and air-in-fluid acoustic systems (Appendix B), which breaks through the limit of the acoustic refractive index and impedance contrast between the background materials and the constituent materials. This excellent characteristic of self-order arrangement will broaden greatly the application scope of topological insulators. We also discuss the trivial rectilinear

modification structures with a winding number corresponding to $n = 0$ without band inversion (Appendix C). In particular, as long as the order parameter maintains its rigidity and the scatterer has C_2 symmetry, the phase transition induced by specific topological modification cannot be removed by smooth, local deformations (Appendix D).

To ascertain the appearance of topologically protected helical edge states for in-plane bulk waves in our system, we combine the radical configuration ($C = 0^\circ$) and the azimuthal configuration ($C = 90^\circ$) to construct a domain wall (highlighted with a dashed red line) [see Fig. 3(a)]. Figure 3(b) shows the simulated projected band structure of a supercell consisting of a total of 20 unit cells in the y direction. As expected, a pair of gapped edge states (shown by blue and red curves) exist evidently inside the overlapped bulk band gap of the two PCs. The two elastic edge states have opposite group velocities at a given frequency, implying the existence of pseudospin-orbit coupling and counterpropagation of edge states. In Fig. 3(c), we plot the simulated field maps of the elastic displacement of edge states corresponding to points A and B, respectively, and both maps show that A and B states are localized at the interface between the nontrivial and the trivial phase.

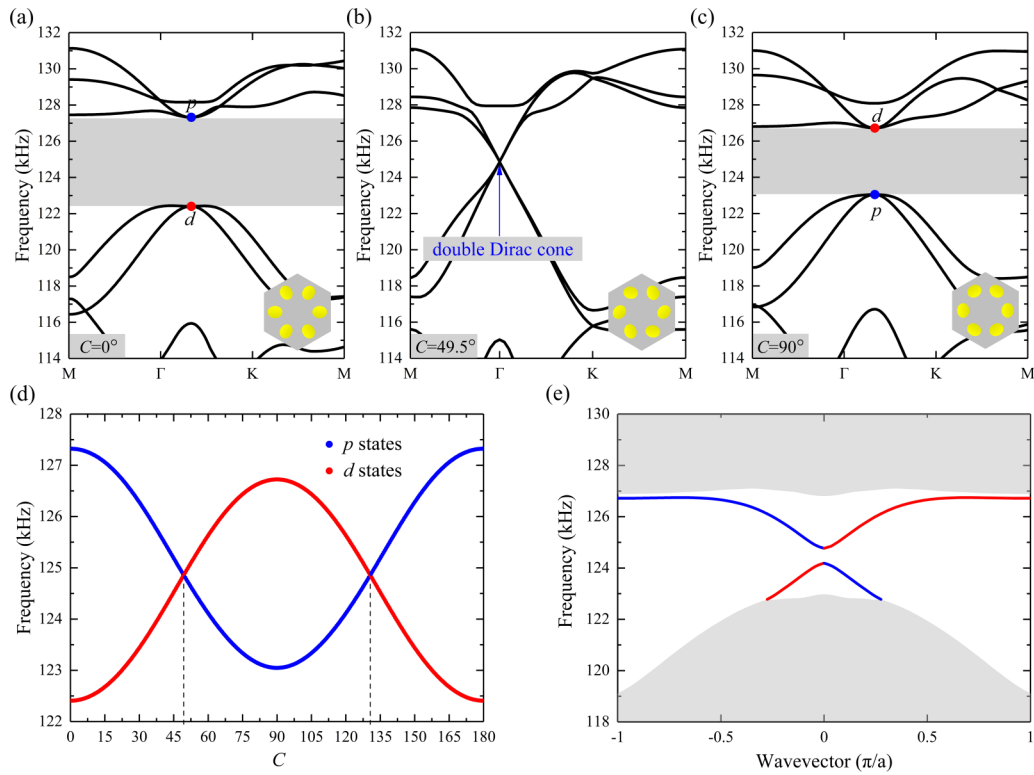


FIG. 5. Band inversion process and topological protected edge states of the elastic PCs constructed by elliptical steel cylinders embedded in an epoxy resin. (a)–(c) Band structure of the elastic PCs with different initial phases with $C = 0^\circ$, 49.5° , and 90° , respectively. Unit cells are depicted at the bottom right corner in each subfigure. The nontrivial crystal in (a) undergoes a topological phase transition, as the band gap closes in (b) and a fourfold-degenerate double Dirac cone is formed at the Γ point, then reopens with an inverted band structure in (c). (d) Eigenfrequencies of the p - and d -type states at the Γ point evolving for a sweep of the initial phase C . The band inversion effect is clearly observed. (e) Calculated band structure of a supercell consisting of a topological nontrivial crystal ($C = 0^\circ$) stacked with a topological trivial crystal ($C = 90^\circ$). The red and blue lines represent an elastic spin+ and spin– edge state, respectively. The shaded regions indicate the bulk states.

Further, the time-averaged mechanical energy flux and its directions (indicated by the black arrows) confirm the existence of the pseudospin-up state (rotates anticlockwise) and the pseudospin-down state (rotates clockwise), which unveils the spin nature of these in-plane modes in the solid PCs. Note that the edge states are gapped and do not completely cross the gap from one bulk band to the other, which suggests that they are not strictly topologically protected in the full frequency band gap. This is because, in our system, the hexagons on each side of the domain wall do not have the same size. Such a sharp interface effectively breaks the C_{6v} symmetry, thereby lifting the spin degeneracy. However, these edge modes are still topological due to the distinct topology of the two surrounding bulks, and the topological edge propagation remains robust. In principle, the small frequency gap at the Γ point can be reduced as the interface we designed is associated with a relatively weak breaking of the C_{6v} symmetry.

IV. SPONTANEOUS SYMMETRY-BREAKING PHASE TRANSITIONS BASED ON DIFFERENT θ -SPACES

The solid system is independent of the molecular numbers in θ -space whose topological phase can be specified by the polar angle φ , which allows for an extension of the phononic

topological phase down to a variety of topological modification structures based on different θ -spaces. To verify this, we investigate the allotropes of a hexagonal non-Bravais lattice containing 12 elliptical tungsten cylinders embedded in an epoxy resin. The lattice constant is $a_s = 15$ mm and $l = 0.3695a_s$. The major axis of the ellipse is $a = 1.2$ mm and the minor axis is $b = 0.6$ mm. Figures 4(a)–4(c) show the band structures of the solid PCs with different initial phases. A fourfold-degenerate double Dirac cone appears at the Γ point of the structure with $C = 22^\circ$. As shown in Figs. 4(a) and 4(c), the p - and d -type states are inverted between two structures, causing energy band inversion. The band gap closing and reopening through Dirac points indicates that the solid PCs experience a topological transition from a topologically trivial crystal ($C = 0^\circ$) to a topologically nontrivial crystal ($C = 45^\circ$). In Fig. 4(d), we show that there are two edge states of opposite velocity in the overlapped bulk band gap when connecting the two PCs of different band topology. The corresponding energy flow profiles at points A and B further confirm the existence of these topologically protected helical edge states. The associated displacement field maps and spatial amplitude profile of the edge states in the y direction are plotted in Fig. 4(e), which shows that the displacement field is concentrated along the domain wall and decays exponentially into the bulk with

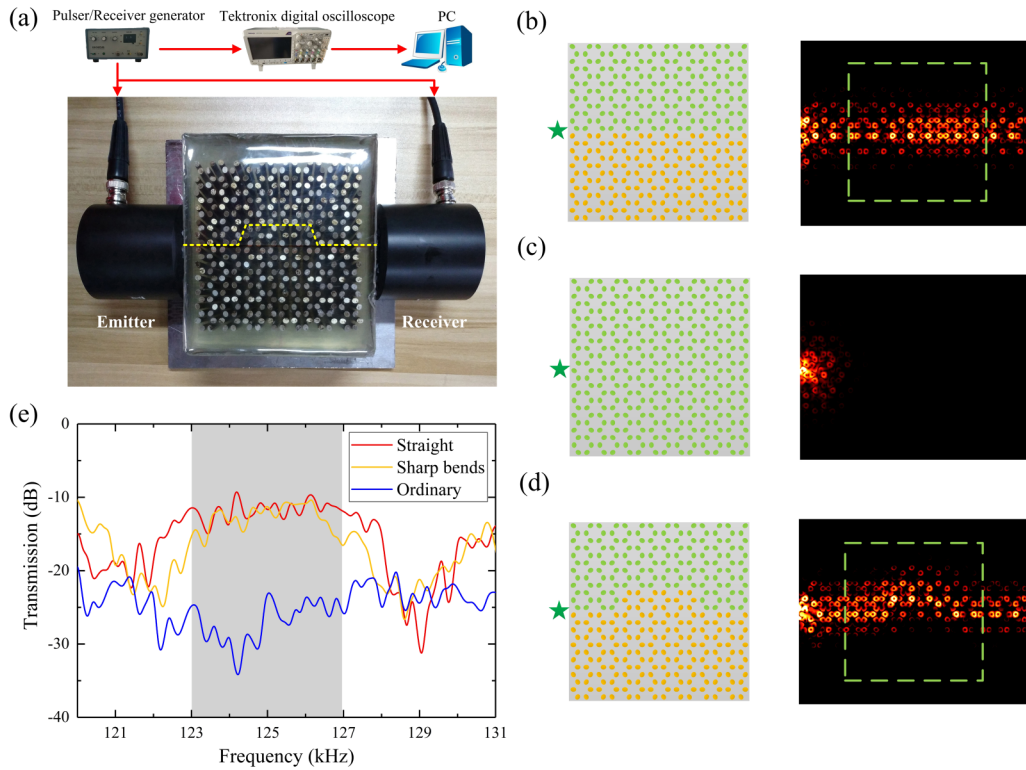


FIG. 6. (a) Photograph of the experiment setup. The yellow dashed lines indicate the location of the waveguides constructed by stacking a topological trivial crystal ($C = 90^\circ$) with a topological nontrivial crystal ($C = 0^\circ$). (b)–(d) Simulated displacement field distribution of the topologically protected waveguide and the ordinary waveguide at a bulk band-gap frequency (125.1 kHz). The green dashed rectangle denotes the region of the area $125 \times 110 \text{ mm}^2$ measured in experiments. Green and orange regions represent the trivial and nontrivial crystals. (e) Experimentally measured transmission spectra for the elastic topologically protected waveguide and the ordinary waveguide. The shaded region corresponds to the topological band gap.

respect to $y = 0$, which is the key characteristic of the edge states. Note that the topological phase transition can also be realized in a double Dirac cone of PCs beyond C_{6v} symmetry (see Appendix E). The overall results hence confirm the high flexibility of this topological modification without the limit of point-group symmetry and the lattice geometry, which clearly distinguishes itself from the conventional methods with the unparalleled advances in practical applications. It is worth emphasizing that our current research is focused on a specific type of topological charge ($k = 1$). Such mapping $\theta = k\varphi + C$ can realize diversified topological orders of phononic states with distinct characteristics by tuning the values of k and φ . Therefore, a tremendous order-parameter space remains to be explored.

V. EXPERIMENTAL DEMONSTRATION OF TRANSPORT ROBUSTNESS

One of the most striking features of the helical edge states is the backscattering-immune one-way propagation and the topological robustness against defects. In the following, we will proceed to an experimental demonstration of these observations. Considering the broad generality of the proposal in an elastic solid, and facilitating the processing and manufacturing of experimental samples, we have investigated the topological properties of in-plane bulk waves in two-dimensional solid PCs

constituted by a triangular array of elliptical steel cylinders embedded in an epoxy resin matrix, obtaining similar results (Fig. 5), and we have further demonstrated experimentally the topological wave propagation. Figure 6(a) shows a picture of the fabricated samples of the elastic topologically protected waveguide (Appendix G). The simulated displacement field distribution of the topologically protected straight waveguide and the ordinary phononic crystal waveguide at a bulk band-gap frequency (125.1 kHz) is illustrated in Figs. 6(b)–6(c) to verify the reflection-free transmission of the helical edge states. It is worth noting that, in comparison with the trivial system alone, in which pure isolation occurs, the in-plane bulk waves transmit along the domain wall without backscattering for the straight waveguide. As shown in Fig. 6(e), the experimental results illustrate the measured ~ 20 dB transmission enhancement of the topological waveguide in contrast to the ordinary waveguide. To further test the robustness of these edge states, we introduce a series of sharp bends to the topologically protected waveguide as shown in Fig. 6(d), and it is observed that there are no notable scattering losses at the structural bends due to the topological protection. The experimentally measured transmission spectra are presented in Fig. 6(e) and demonstrate no significant elastic transmission drops within the bulk band-gap frequency region by comparing with the results of the straight waveguide. The overall lower transmission intensity in the power spectrum can be attributed

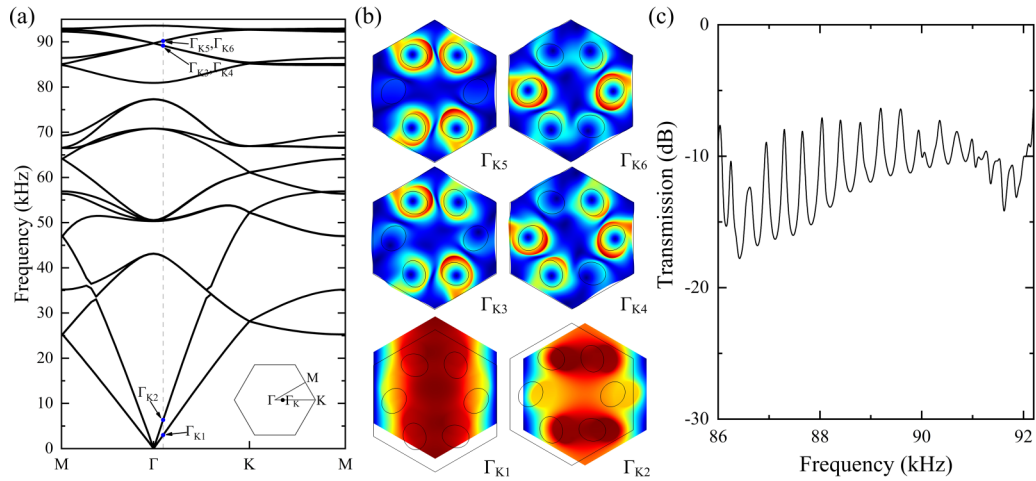


FIG. 7. (a) Calculated band structure in which $C = 47.5^\circ$. (b) The associated model displacement trajectories (near the Γ point). (c) Simulated transmission spectra in the frequency range of the four degeneracy bands with longitudinal input excitation.

to the conversion of a transverse wave to a longitudinal wave. Thus, our edge states exhibit topological protection against certain disorder and defects, demonstrating the absence of backscattering and resulting in the inherently robust one-way propagation of in-plane bulk waves.

VI. CONCLUSION

In conclusion, we have designed a unique elastic topological insulator based on a topological modification in a triangular lattice of elliptical cylinders, whose multiple topological phase

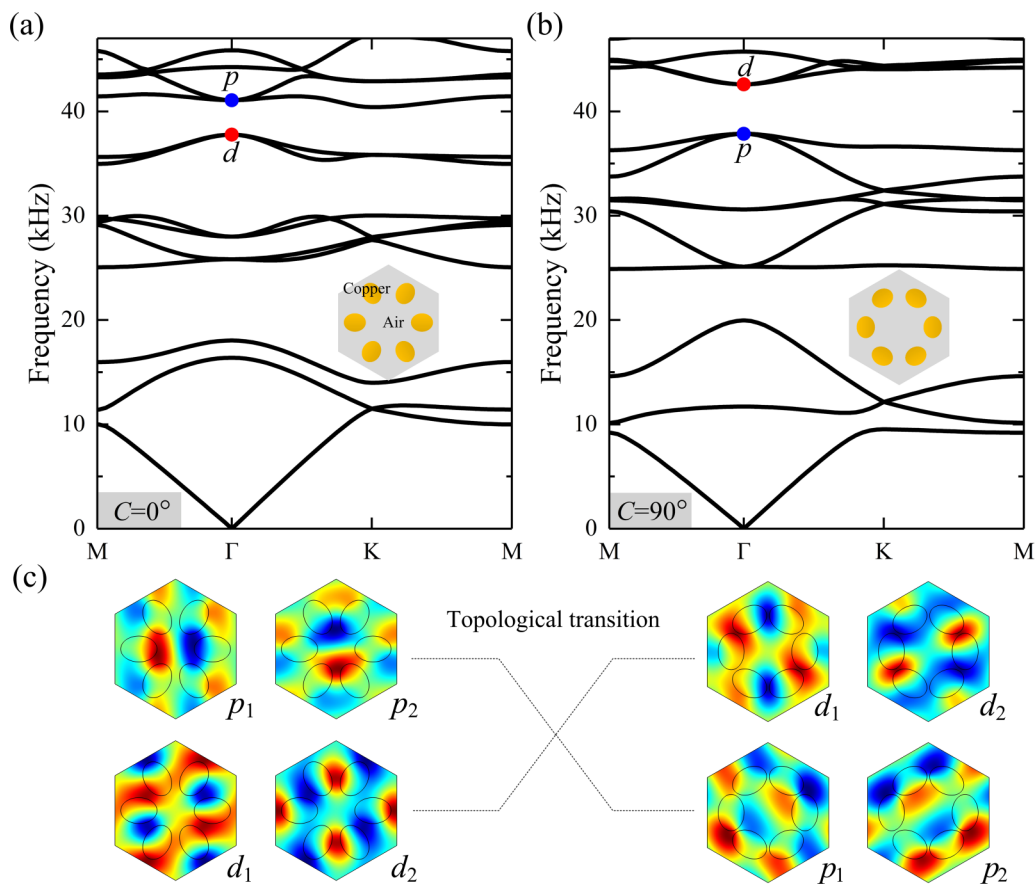


FIG. 8. Acoustic pseudospin states and band inversion process in a solid-in-air system, in which the phononic crystal structure consisting of elliptical copper cylinders is embedded in air. (a),(b) Band structures of the PCs with different initial phases with $C = 0^\circ$ and 90° , respectively. Unit cells are depicted at the right corner in each subfigure. The lattice constant $a_s = 15$ mm and the distance between the adjacent cylinders $l = 0.3030a_s$. The major axis of the ellipse is $a = 2.2481$ mm and the minor axis is $b = 1.6085$ mm. (c) The band inversion underlying the topological transition from nontrivial phases to trivial phases upon changing the initial phase C .

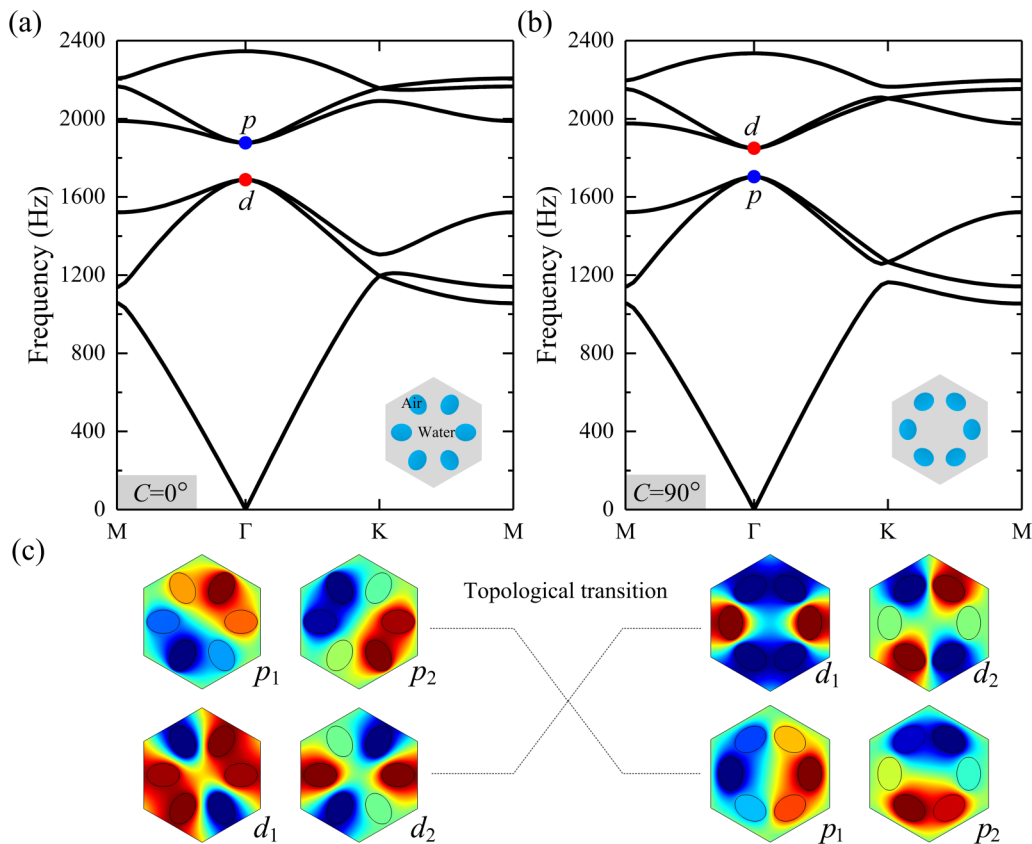


FIG. 9. Acoustic pseudospin states and band inversion process in an air-in-fluid system, in which the phononic crystal structure consisting of elliptical cylinders filled with air is embedded in water. (a),(b) Band structures of the PCs with different initial phases with $C = 0^\circ$ and 90° , respectively. Unit cells are depicted at the bottom right corner in each subfigure. The lattice constant $a_s = 15$ mm and the distance between the adjacent cylinders $l = a_s/3$. The major axis of the ellipse is $a = 2.1$ mm and the minor axis is $b = 1.5$ mm. (c) The band inversion underlying the topological transition from nontrivial phases to trivial phases upon changing the initial phase C .

transitions can be realized by inhomogeneously changing the ellipse orientation within the unit cells. Robust one-way propagation for in-plane bulk waves and the ability to guide waves along channels with sharp bends in the solid PCs is experimentally verified. Interestingly, the solid system with spontaneously broken symmetry is independent of the number of molecules in order-parameter space, providing the possibility for achieving a new form of topological wave propagation beyond C_{6v} symmetry. Such a topological modification is much different from conventional methods to obtain a topological phononic phase in condensed-matter physics, which allows us to explore fundamentally new physics beyond the original physics via various order-parameter spaces. Moreover, the methods can be directly extended to other classic wave such as electromagnetic and plate-mode waves. We believe that our demonstrated elastic topological phenomena open a new avenue for manipulating and transporting in-plane bulk waves, which can be of immense value for practical applications.

ACKNOWLEDGMENTS

This work is supported by the National Science Foundation of China (Grants No. 11374093 and No. 11672214), and the

Young Scholar fund sponsored by the common university and college of the province in Hunan.

J.-J.C. and H.-B.H. contributed equally to this work.

APPENDIX A: POLARIZATION CHARACTERISTICS

To better understand the polarization of the in-plane mode in our solid system, we plot the band structure of the accidental degeneracy point and the corresponding model displacement trajectories (near the Γ point) as illustrated in Figs. 7(a) and 7(b), respectively. It is observed that, in the low-frequency regime (near the Γ point), the first and second bands correspond to transverse and longitudinal modes, respectively, while for high frequency all modes are found to have mixed longitudinal-transverse polarization [43]. Figure 7(c) presents the simulated transmission spectra in the four degeneracy bands frequency range with longitudinal input excitation, and the lower transmission rate can be attributed to the conversion of transverse wave to longitudinal wave. These results, therefore, demonstrate that the four degeneracy bands constructed double Dirac cones are the mixed longitudinal-transverse polarization modes dominated by transverse polarization.

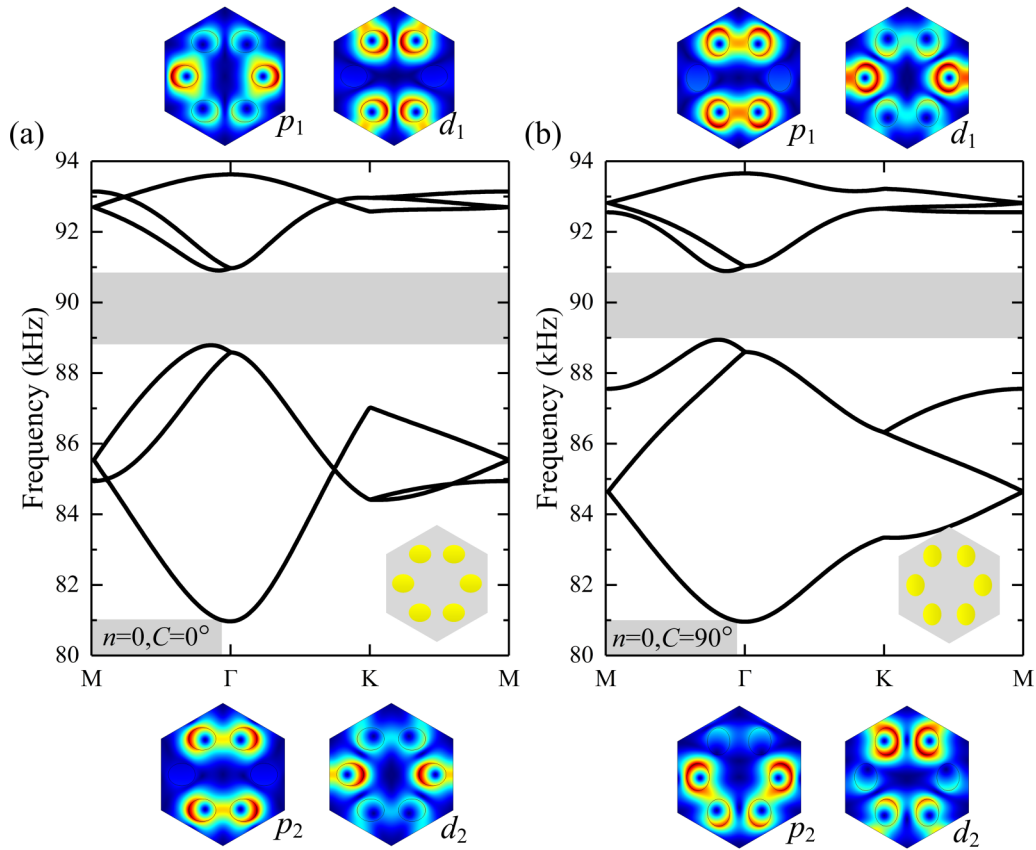


FIG. 10. Band structures of the trivial rectilinear modification structures and the associated displacement field distributions for the degenerate eigenstates at the Γ point. Band inversion no longer takes place since there is no reversal between the p - and d -type states with respect to the band gap. Unit cells are depicted at the bottom right corner in each subfigure. The shaded regions indicate the complete band gap.

APPENDIX B: THE BROAD GENERALITY OF THE TOPOLOGICAL MODIFICATION IN PRACTICAL SYSTEMS

To further verify the generality and maneuverability in practical observation, we demonstrate that the topological modification in the orientational order can be directly extended to other classic waves, such as solid-in-air and air-in-fluid acoustic systems. Figure 8 shows the corresponding topological phase transition with p/d -like band inversion in the triangular lattice of hexagonal clusters composed of six elliptical copper cylinders embedded in air. Here, the copper is described as a rigid material and has a higher acoustic impedance contrast than air (8900×4710 versus 1.25×343). As shown in Figs. 8(a)–8(c), an accidental double Dirac cone is formed at the Γ point, and the topological nontrivial state changes to a trivial state upon changing the initial phase C . Figure 8(d) demonstrates the topological p/d -like band inversion underlying the transition. In contrast to the solid-in-air system, the air is assumed to be a soft material with respect to water and has a higher acoustic refractive index than water ($1480/343$ versus 1), and we found that the air-in-fluid system also maintains a topological transition, which is shown in Fig. 9. The topological modification provides insights into the mechanism of band control to surpass the limits of the acoustic refractive index and impedance contrast between the

background materials and the constituent materials, which have a wide range of applicability in acoustic systems.

APPENDIX C: THE TRIVIAL RECTILINEAR MODIFICATION STRUCTURES WITH $n = 0$

As shown in Fig. 10, the shrinking (or expanding) of the background medium region between two adjacent elliptical cylinders results in the opening of a trivial band gap. However, the band inversion and topological phase transition cannot occur in the trivial rectilinear modification structures because the modification of the unit cell that breaks the rotational symmetry does not change the topology of the structure. Thus, the $n = 0$ trivial rectilinear structure is said to be topologically unstable, which further indicates that the topologically stable structure with $n = +1$ is more specifically suited to induce the phase transition as compared to $n = 0$.

APPENDIX D: BAND INVERSION PROCESS WITH RECTANGULAR CYLINDERS

Here, we consider the solid PCs composed of rectangular cylinders with C_2 symmetry. As shown in Fig. 11, the similar band inversion effect can be induced as long as the order parameter maintains its rigidity.

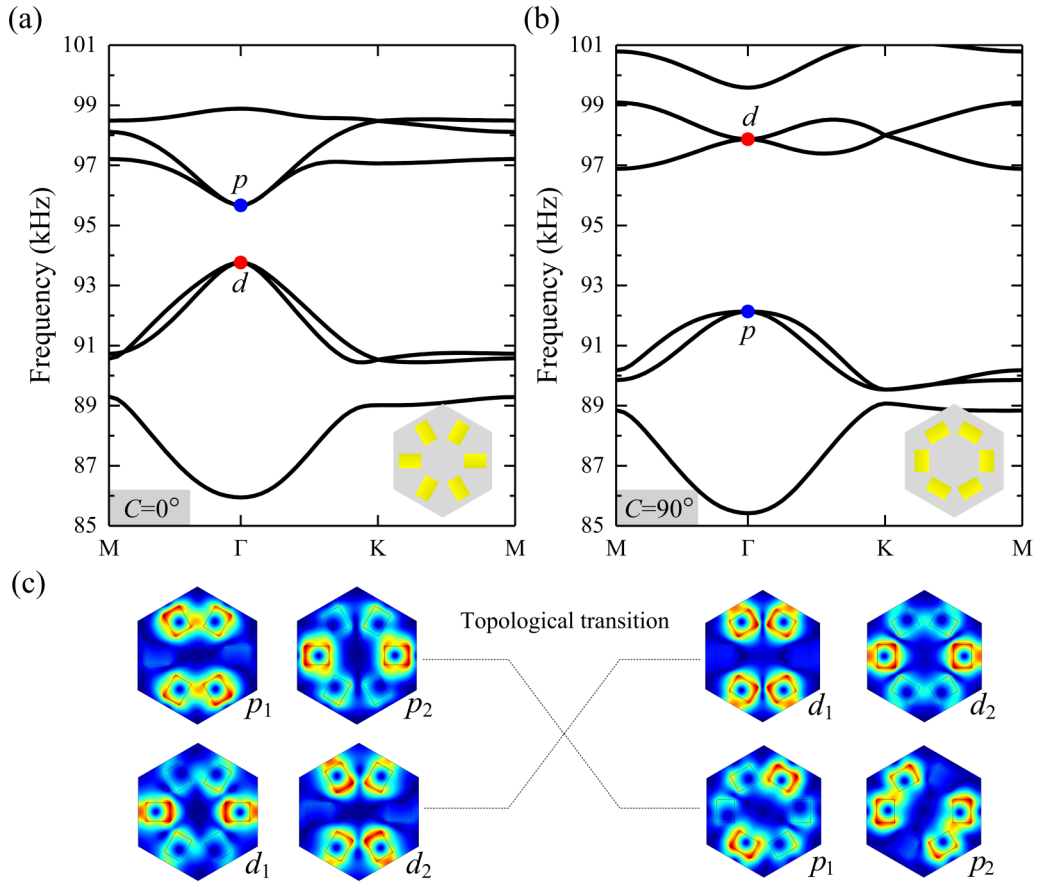


FIG. 11. Topological mode inversion between the elastic PCs consisting of rectangular tungsten cylinders embedded in an epoxy resin matrix. (a),(b) Band structures of the PCs with different initial phases with $C = 0^\circ$ and 90° , respectively. Unit cells are depicted at the bottom right corner in each subfigure. The lattice constant $a_s = 15$ mm and the distance between the adjacent cylinders $l = a_s/3$. The length and width of the rectangle is $a = 3.0314$ mm and $b = 2.3318$ mm, respectively, whose filling ratio is identical with the elliptical tungsten cylinders in the main text. (c) The band inversion underlying the topological transition from nontrivial phases to trivial phases upon changing the initial phase C .

APPENDIX E: BAND INVERSION PROCESS BEYOND C_{6v} SYMMETRY

As demonstrated in the main text, our system is independent of the molecular numbers in θ -space, which allows for an extension of the phononic topological phase down to various point-group symmetries. As illustrated in Fig. 12, we plot the band structures of the PCs consisting of 15 elliptical cylinders, and the band inversion is clearly observed by varying the initial phase C . Different from the previous proposals [32,33] to generate the double Dirac cone at the Γ point based on C_{6v} symmetry, our approach breaks through the limit of the point-group symmetry to emulate pseudospin-orbit coupling without relying on tuning the filling ratio or folding the Brillouin zone.

APPENDIX F: SIMULATION

All full-wave simulations presented in this paper are performed using commercial finite-element method software COMSOL MULTIPHYSICS, a solid mechanics module, and a pressure acoustics module. The material parameters used for calculation are $\rho = 19\,100$ kg/m³, $E = 354.1$ GPa, $\sigma = 0.35$ for tungsten, $\rho = 1180$ kg/m³, $E = 4.35$ GPa, and $\sigma = 0.368$ for epoxy, where ρ , E , and σ are the density, Young modulus,

and Poisson ratio, respectively. When calculating the bulk (edge) band structure, Floquet periodic boundary conditions are imposed on periodic surfaces of the unit cell (supercell), and the elastic phononic crystal structures are surrounded by perfectly matched layers (PMLs) so that there is no reflected wave from the boundaries of the simulation domains.

APPENDIX G: EXPERIMENTAL SETUP

The samples consist of elliptical stainless-steel rods with the major axis $a = 1.85$ mm and the minor axis $b = 1.55$ mm, embedded in an epoxy resin. The lattice constant is $a_s = 15$ mm and the total size of the samples is 125 mm \times 110 mm \times 65 mm. In experiments, a couple of ultrasonic broadband transducers with a central frequency of 100 kHz and a diameter of 60 mm (OLYMPUS contact transducers type Videoscan No. V1011) are used to act as the emitter and the receiver, launching a probing longitudinal wave signal from the emitter through the composite sample, which is then processed at the receiver. The emitter is centered on the transversal face of the sample, and the nearly parallel signal is perpendicular to the cylinders. Both emitter and receiver are coupled to the transversal face using a coupling gel. The emitter is excited with

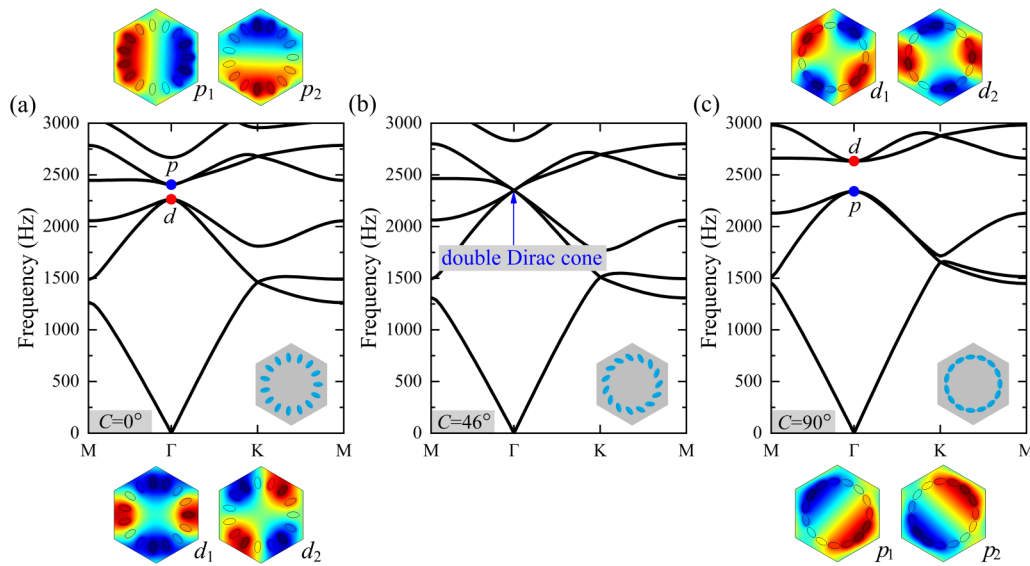


FIG. 12. Topological phase transition and band inversion process in an air-in-fluid system beyond C_{6v} symmetry, in which the phononic crystal structure consisting of 15 elliptical cylinders filled with air is embedded in water. (a)–(c) Band structures of the PCs with different initial phases with $C = 0^\circ$, 46° , and 90° , respectively. A double Dirac cone is seen at the Γ point. Unit cells are depicted at the bottom right corner in each subfigure. The lattice constant $a_s = 15$ mm and the distance between the adjacent cylinders $l = 0.3829a_s$. The major axis of the ellipse is $a = 1.06$ mm and the minor axis is $b = 0.53$ mm. The band inversion underlying the topological transition from nontrivial phases to trivial phases upon changing the initial phase C .

an ultrasonic emission source (OLYMPUS model 5073PR) producing a short-duration large-amplitude pulse. The signal acquired by the receiver is postamplified and then digitized

with a Tektronix digital oscilloscope with real-time fast Fourier transform (FFT) capability to produce the transmission power spectrum.

-
- [1] N. D. Mermin, *Rev. Mod. Phys.* **51**, 591 (1979).
 [2] M. Kleman, and O. D. Lavrentovich, *Soft Matter Physics: An Introduction* (Springer, New York, 2003).
 [3] R. Podgornik, *J. Stat. Phys.* **83**, 1263 (1996).
 [4] V. Pal, C. Tradonsky, R. Chriki, A. A. Friesem, and N. Davidson, *Phys. Rev. Lett.* **119**, 013902 (2017).
 [5] T. W. B. Kibble, *J. Phys. A* **9**, 1387 (1976).
 [6] W. H. Zurek, *Nature (London)* **317**, 505 (1985).
 [7] T. B. Saw, A. Doostmohammadi, V. Nier, L. Kocgozlu, S. Thampi, and Y. Toyama *et al.*, *Nature (London)* **544**, 212 (2017).
 [8] K. Kawaguchi, R. Kageyama, and M. Sano, *Nature (London)* **545**, 327 (2017).
 [9] G. Duclos, C. Erlenkämper, J. F. Joanny, and P. Silberzan, *Nat. Phys.* **13**, 58 (2017).
 [10] I. Kolvin, G. Cohen, and J. Fineberg, *Nat. Mater.* **17**, 140 (2018).
 [11] L. L. Van, T. Shimada, J. Wang, and T. Kitamura, *Nanoscale* **9**, 15525 (2017).
 [12] F. D. M. Haldane and S. Raghu, *Phys. Rev. Lett.* **100**, 013904 (2008).
 [13] Z. Wang, Y. D. Chong, J. D. Joannopoulos, and M. Soljčić, *Phys. Rev. Lett.* **100**, 013905 (2008).
 [14] Z. Wang, Y. Chong, J. D. Joannopoulos, and M. Soljčić, *Nature (London)* **461**, 772 (2009).
 [15] M. Hafezi, E. A. Demler, M. D. Lukin, and J. M. Taylor, *Nat. Phys.* **7**, 907 (2011).
 [16] M. Hafezi, S. Mittal, J. Fan, A. Migdall, and J. M. Taylor, *Nat. Photon.* **7**, 1001 (2013).
 [17] Y. Poo, R.-X. Wu, Z. Lin, Y. Yang, and C. T. Chan, *Phys. Rev. Lett.* **106**, 093903 (2011).
 [18] K. Fang, Z. Yu, and S. Fan, *Nat. Photon.* **6**, 782 (2012).
 [19] M. C. Rechtsman *et al.*, *Nature (London)* **496**, 196 (2013).
 [20] A. B. Khanikaev *et al.*, *Nat. Mater.* **12**, 233 (2013).
 [21] L.-H. Wu and X. Hu, *Phys. Rev. Lett.* **114**, 223901 (2015).
 [22] T. Ma, A. B. Khanikaev, S. H. Mousavi, and G. Shvets, *Phys. Rev. Lett.* **114**, 127401 (2015).
 [23] W. J. Chen, S. J. Jiang, X. D. Chen, B. Zhu, L. Zhou, and J. W. Dong *et al.*, *Nat. Commun.* **5**, 5782 (2014).
 [24] V. Peano, C. Brendel, M. Schmidt, and F. Marquardt, *Phys. Rev. X* **5**, 031011 (2015).
 [25] M. Xiao, Z. Q. Zhang, and C. T. Chan, *Phys. Rev. X* **4**, 021017 (2014).
 [26] M. Xiao *et al.*, *Nat. Phys.* **11**, 240 (2015).
 [27] Z. Yang *et al.*, *Phys. Rev. Lett.* **114**, 114301 (2015).
 [28] X. Ni *et al.*, *New J. Phys.* **17**, 053016 (2015).
 [29] Z. G. Chen and Y. Wu, *Phys. Rev. Appl.* **5**, 054021 (2016).
 [30] A. B. Khanikaev, R. Fleury, S. H. Mousavi, and A. Alu, *Nat. Commun.* **6**, 8260 (2015).
 [31] Y. Zhu, Y. Peng, X. Fan, J. Yang, B. Liang, X. Zhu *et al.*, [arXiv:1801.07942](https://arxiv.org/abs/1801.07942).
 [32] C. He, X. Ni, H. Ge, X. C. Sun, Y. B. Chen, M. H. Lu, X. P. Liu, and Y. F. Chen, *Nat. Phys.* **12**, 1124 (2016).
 [33] Z. Zhang, Q. Wei, Y. Cheng, T. Zhang, D. Wu, and X. Liu, *Phys. Rev. Lett.* **118**, 084303 (2017).

- [34] Y. Deng, H. Ge, Y. Tian, M. Lu, and Y. Jing, *Phys. Rev. B* **96**, 184305 (2017).
- [35] J. Mei, Z. Chen, and Y. Wu, *Sci. Rep.* **6**, 32752 (2016).
- [36] Y. G. Peng, C. Z. Qin, D. G. Zhao, Y. X. Shen, X. Y. Xu, and M. Bao *et al.*, *Nat. Commun.* **7**, 13368 (2016).
- [37] J.-Y. Lu *et al.*, *Nat. Phys.* **13**, 369 (2017).
- [38] J. Lu, C. Qiu, M. Ke, and Z. Liu, *Phys. Rev. Lett.* **116**, 093901 (2016).
- [39] J. Lu, C. Qiu, W. Deng, X. Huang, F. Li, F. Zhang, S. Chen, and Z. Liu, *Phys. Rev. Lett.* **120**, 116802 (2018).
- [40] M. Xiao, W. J. Chen, W.-Y. He, and C. T. Chan, *Nat. Phys.* **11**, 920 (2015).
- [41] S. H. Mousavi, A. B. Khanikaev, and Z. Wang, *Nat. Commun.* **6**, 8682 (2015).
- [42] E. Prodan and C. Prodan, *Phys. Rev. Lett.* **103**, 248101 (2009).
- [43] P. Wang, L. Lu, and K. Bertoldi, *Phys. Rev. Lett.* **115**, 104302 (2015).
- [44] L. M. Nash, D. Kleckner, A. Read, V. Vitelli, A. M. Turner, and W. T. Irvine, *Proc. Natl. Acad. Sci. (U.S.A.)* **112**, 14495 (2015).
- [45] N. Swinckel, S. Matsuo, K. Runge, J. O. Vasseur, P. Lucas, and P. A. Deymier, *J. Appl. Phys.* **118**, 063103 (2015).
- [46] R. Süsstrunk and S. D. Huber, *Science* **349**, 47 (2015).
- [47] C. L. Kane and T. C. Lubensky, *Nat. Phys.* **10**, 39 (2014).
- [48] R. K. Pal and M. Ruzzene, *New J. Phys.* **19**, 025001 (2017).
- [49] T. W. Liu and F. Semperlotti, *Phys. Rev. Appl.* **9**, 014001 (2018).
- [50] H. Zhu, T. W. Liu, and F. Semperlotti, *Phys. Rev. B* **97**, 174301 (2018).
- [51] J. Vila, R. K. Pal, and M. Ruzzene, *Phys. Rev. B* **96**, 134307 (2017).
- [52] Y. Wu, R. Chaunsali, H. Yasuda, K. Yu, and J. Yang, *Sci. Rep.* **8**, 112 (2018).
- [53] R. Chaunsali, C. W. Chen, and J. Yang, *Phys. Rev. B* **97**, 054307 (2018).
- [54] S.-Y. Yu, C. He, Z. Wang, F.-K. Liu, X.-C. Sun, Z. Li, M.-H. Lu, X.-P. Liu, and Y.-F. Chen, [arXiv:1707.04901](https://arxiv.org/abs/1707.04901).
- [55] J. J. Chen, S. Y. Huo, Z. G. Geng, H. B. Huang, and X. F. Zhu, *AIP Adv.* **7**, 115215 (2017).
- [56] J. Li, J. Wang, S. Wu, and J. Mei, *AIP Adv.* **7**, 125030 (2017).
- [57] S. Y. Huo, J. J. Chen, H. B. Huang, and G. L. Huang, *Sci. Rep.* **7**, 10335 (2017).
- [58] S. Y. Huo, J. J. Chen, and H. B. Huang, *J. Phys.: Condens. Matter* **30**, 145403 (2018).
- [59] Y. Guo, T. Dekorsy, and M. Hettich, *Sci. Rep.* **7**, 18043 (2017).